Nano Research

Open Access

Research Article

# Single-atom Pt anchored $In_2O_3$ nanorods for sensitive acetone detection using early fire warning

Jingmin Ge[1], Zhichuang Ma[1], Jingfang Ji[2], Ruipeng Wang[1], Hao Gao[1], Kaihang Sun[3], Pan Liu[1] ✉, Guochen Qi[1] ✉, and Ronghan Wei[1] ✉

[1] *School of Mechanics and Safety Engineering, Henan Province Engineering Technology Research Center of MEMS Manufacturing and Applications, Industrial Technology Research Institute, Zhengzhou University, Zhengzhou 450001, China*
[2] *Key Laboratory of Automotive Power Train and Electronic Control, Hubei University of Automotive Technology, Shiyan 442002, China*
[3] *College of Chemistry, Zhengzhou University, Zhengzhou 450001, China*

**Cite this article:** *Nano Research*, **2026**, *19*, 94908507. https://doi.org/10.26599/NR.2026.94908507

**ABSTRACT:** The development of high-performance gas sensors is crucial for applications in environmental monitoring, public safety, and healthcare. However, existing analytical techniques are often limited by high costs and operational complexity. $In_2O_3$ semiconductors exhibit great potential, while their practical application is hindered by inherent issues such as sensitivity and selectivity. Herein, we synthesized $In_2O_3$ with oxygen vacancies ($In_2O_3$-L) and anchored Pt single atoms, enabling real-time detection of low-concentration acetone. The $In_2O_3$-L-Pt sensor demonstrated a 5-fold improvement in response to 20 ppm acetone at 220 °C compared to $In_2O_3$, exhibiting rapid response/recovery time (2/30 s), ultra-low theoretical detection limits, excellent selectivity, and outstanding long-term stability. Experimental and theoretical results indicated that Pt single atoms enhanced adsorption and reduced activation energy barrier. Importantly, the Pt induced an internal electric field, increasing the thickness of the electron depletion layer (EDL), thereby amplifying the electrical response. This work demonstrates the potential of single-atom engineering to overcome the limitations of metal oxide sensors and presentes a new approach for designing next-generation portable sensing devices. Moreover, the sensor demonstrates practical application potential, as shown in simulated automotive fire-warning scenarios.

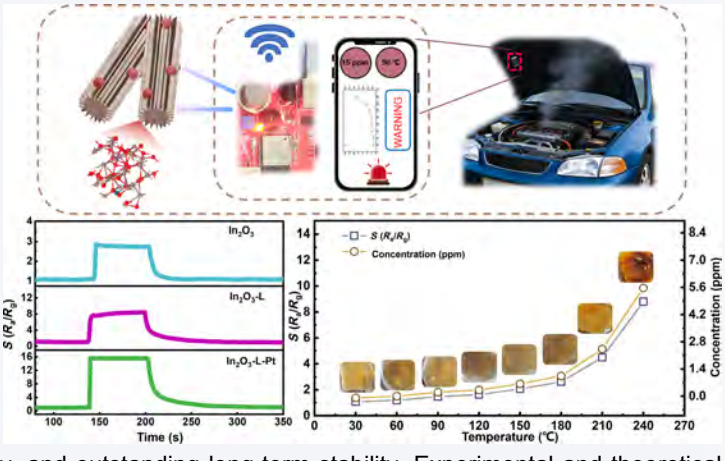


**KEYWORDS:** metal oxide sensors, $In_2O_3$, single atoms, high selectivity, fire-warning scenarios

## 1 Introduction

Highly sensitive, selective, and stable gas sensors are significant importance for a wide range of applications, including public security, environmental monitoring, health diagnostics, and industrial and agricultural production. Conventional analytical techniques, such as gas chromatography-mass spectrometry (GC-MS) [1], proton transfer reaction-mass spectrometry (PTR-MS) [2], and Fourier transform infrared (FT-IR) spectrometry [3], could accurately detect trace gases. However, the use of these devices is often hindered by high costs, complex operation procedures, and the cumbersome nature of the equipment. Metal oxide semiconductor (MOS)-based gas sensors present a compelling alternative due to the low cost, facile fabrication, simple operation, and ease of miniaturization for device integration [4–6].

Indium oxide ($In_2O_3$), as a typical semiconductor material for gas sensors, has garnered significant attention due to its tunable wide bandgap (~ 3.6 eV), excellent chemical stability, and high intrinsic electron mobility. These characteristics enable $In_2O_3$ to exhibit excellent sensing performance for a variety of target gases [7, 8], such as nitrogen dioxide ($NO_2$), carbon monoxide (CO), and ammonia ($NH_3$), making it one of the preferred candidate materials

**Received:** December 19, 2025; **Revised:** January 22, 2026
**Accepted:** January 29, 2026

✉Address correspondence to Pan Liu, newpan@zzu.edu.cn; Guochen Qi, qigc@zzu.edu.cn; Ronghan Wei, Profwei@zzu.edu.cn

for the next generation of resistive sensors. However, despite its excellent theoretical gas sensing performance, the practical application of $In_2O_3$ is still limited by issues such as insufficient sensitivity, slow response dynamics, and poor gas selectivity. To address the problems, strategies such as doping [9–11] (e.g., Pd, Au, and Ni), creating vacancies [12–14], and nano-structuring (e.g., particle or rod-like forms) have been employed to increase the surface area and modulate the electronic structure [15, 16], thereby enhancing the sensing performance. Although these approaches have improved the sensing capabilities and stability of $In_2O_3$, they usually only bring limited improvement effects. Consequently, there is an urgent need for a transformation in the design of gas sensing materials, shifting from rough adjustments in form or composition to more precise atomic-level interface engineering construction [17–19]. Single-atom catalysis, as an emerging frontier technology, offers new opportunities to maximize the utilization of active sites and create highly localized electric fields, potentially unlocking the full theoretical gas sensing potential of $In_2O_3$ and opening new directions in the design of gas sensing materials.

Based on the above discussion, we prepared $In_2O_3$ nanorods with oxygen vacancies ($In_2O_3$-L) via a hydrothermal method, and anchored Pt single atoms using a precipitation method. To investigate the improvement in sensor response of single-atoms Pt, gas sensing tests were conducted on $In_2O_3$-L-Pt composites. Experimental results revealed that the sensor response of $In_2O_3$-L-Pt (response value: 17) was 5 times higher than that of $In_2O_3$, and the response/recovery time was 2/30 s, respectively. This material exhibits superior sensing performance compared to the sensors reported in related literature (Table S1 in the Electronic Supplementary Material (ESM)). To further explore the reasons for the enhanced sensing performance, density functional theory (DFT) calculations were performed. These results demonstrated that the Pt single atoms increased the adsorption and reduced activation energy barrier, facilitating electronic interactions between Pt and $In_2O_3$-L. This work provides new insights into the development of portable sensors, offering promising applications in fire warning and real-time monitoring systems.

## 2 Experimental

### 2.1 Synthesis of $In_2O_3$ and $In_2O_3$-L

5.0 g (82.51 mM) of urea and 0.6 g (1.54 mM) of $In(NO_3)_3{\cdot}5H_2O$ were dissolved in 20 mL of deionized water to form a homogeneous solution. A white precipitate was obtained after 4 h of water bath reaction at 80 °C. The sample was washed several times with deionized water and ethanol, and then dried at 60 °C in an oven to obtain the white powders of $In(OH)_3$. $In(OH)_3$ was calcined at 250 °C in an air atmosphere at a heating rate of 2 °C/min for 2 h, resulting in rod-shaped $In_2O_3$, denoted as $In_2O_3$-L.

For comparison, $In_2O_3$ powders were prepared by directly annealing 1.0 g (2.56 mM) of $In(NO_3)_3{\cdot}5H_2O$ at 250 °C in an air atmosphere at a heating rate of 2 °C/min for 2 h.

### 2.2 Synthesis of $In_2O_3$-L-Pt

0.5 g (1.28 mM) as-prepared $In_2O_3$-L and 0.035 g (0.085 mM) of $H_2PtCl_6$ were dissolved in 160 mL of deionized water. The mixture solution was reacted in a water bath at 80 °C for 1 h, and then 0.125 g (2.06 mM) of urea was added and the reaction was continued for another 3 h. The light-yellow precipitate was collected, washed several times, and dried to obtain Pt-loaded $In_2O_3$, denoted as $In_2O_3$-L-Pt-1.

The doses of $H_2PtCl_6$ and the urea were respectively increased by 2, 6, and 10 times, and the obtained materials were labeled as $In_2O_3$-L-Pt-2 (signed as $In_2O_3$-L-Pt), $In_2O_3$-L-Pt-3, and $In_2O_3$-L-Pt-4.

### 2.3 Material characterization

The morphologies and structural features of the samples were characterized by field-emission scanning electron microscopy (FE-SEM, JEOL JSM-7610F) and high-resolution transmission electron microscopy (HRTEM, FEI Tecnai F30 at 300 kV). The atom distribution was analyzed using high-angle annular dark field image-scanning transmission electron microscopy (HAADF-STEM). The element contents of the materials were analyzed by energy dispersive X-ray spectroscopy (EDS) mapping and inductively coupled plasma optical emission spectrometry (ICP-OES). The crystal structure of the samples was determined by X-ray diffraction (XRD, PANalytical, Cu K$\alpha$ radiation), while the surface chemical states were examined via X-ray photoelectron spectroscopy (XPS, Thermo Scientific ESCALAB 250Xi, Al K$\alpha$ source).

### 2.4 Fabrication of the gas sensor

The above obtained samples (about 20 mg) were mixed with 500 μL of ethanol to form a uniform slurry, which was uniformly coated onto an alumina ceramic tube containing the gold electrode. The coated electrode components were aged in a muffle furnace at 300 °C at a heating rate of 3 °C/min for 12 h. A gas sensor was fabricated by connecting the electrodes to a base socket via Pt wires. The sensing performance was evaluated using a CGS-8 gas-sensing analysis system (Beijing Elite Tech Co., Ltd.) (Fig. S1 in the ESM). Gas atmospheres of various concentrations were prepared using a micro-sampling needle. The equation for calculating gas concentration was as follows

$$C = \frac{V_m \times d \times \rho \times Q}{V \times M} \quad (1)$$

where $C$ is the concentration of the target gases (ppm), $V_m$ is the molar volume of gas (L/mol), $d$ is the purity values of all target liquid, $\rho$ is the density of the liquid samples (kg/m$^3$), $Q$ is the volume of the target liquid (L), $V$ is the volume of the air chamber (L), and $M$ is the molecular weight of the target gas (g/mol).

During the testing process, all the sensors exhibited n-type semiconductor characteristics. Here, the sensor response ($S$) was defined as

$$S = \frac{R_a}{R_g} \quad (2)$$

where $R_a$ is the resistance value of the sensor in the air, and $R_g$ is the resistance value of the sensor exposed to the target gas.

The time required for the sensor signal to reach 90% of its total change in the target gas or in air was defined as the response time and recovery time, respectively.

## 3 Results and discussion

### 3.1 Synthesis and characterization

The preparation process of the sensor materials is shown in Fig. 1 (the specific experimental details could be found in Section 2). The structure and morphology of the samples were investigated by

scanning electron microscopy (SEM) and transmission electron microscopy (TEM). $In_2O_3$ prepared by the traditional method presented a block-like structure (Fig. 2(a)). The nano-rod structure of $In_2O_3$-L was prepared by water bath method. The length of the rod was about 300–500 nm, and the diameter was about 30 nm (Figs. 2(b) and 2(c)). The nano-rod $In_2O_3$-L remained virtually unchanged after Pt modification (Fig. S2 in the ESM). The atomic arrangements of In, Pt, and O in $In_2O_3$-L-Pt was further characterized by HAADF-STEM. The intensity in HAADF-STEM images is directly proportional to the atomic number. Pt atoms appeared brighter than In and O, whereas in atoms were darker, and all metal atoms exhibited greater intensity than the O atoms (Fig. 2(d)). Atomic-scale bright dots abounded on the $In_2O_3$ substrate. Higher-magnification images confirmed the presence of uniformly distributed Pt single-atoms (Figs. 2(e) and 2(f)). The TEM image further indicated that $In_2O_3$-L had a highly uniform rod-like structure. Figure S3 in the ESM indicated the lattice spacing of 0.286 nm, which was assigned to the (222) lattice fringes of $In_2O_3$. The mapping diagrams confirmed that the elements of In, O, and Pt were uniformly distributed throughout the material, and the single-atoms Pt were evenly distributed on $In_2O_3$ (Fig. 2(g)).

The structures of the synthesized samples were examined by XRD (Fig. 3(a)). The XRD spectra showed the diffraction peaks at 30.6°, 35.5°, 51.2°, and 60.7°, which corresponded to the (222), (400), (433), and (631) crystal planes of $In_2O_3$, respectively (PDF #71-2195), indicating that the $In_2O_3$ was successfully prepared. The diffraction peaks of $In_2O_3$ after loading Pt remained unchanged. No peaks related to Pt were observed, indicating that there were no Pt

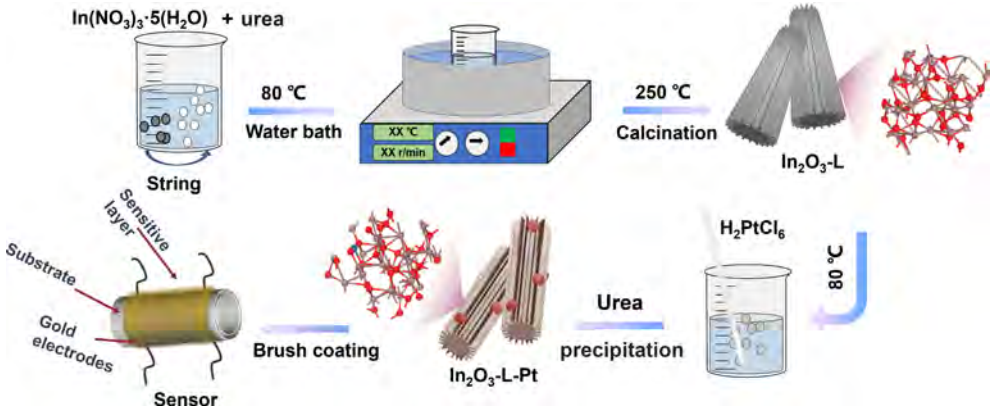


**Figure 1** Schematic illustration of $In_2O_3$-L-Pt synthesis and sensor fabrication.

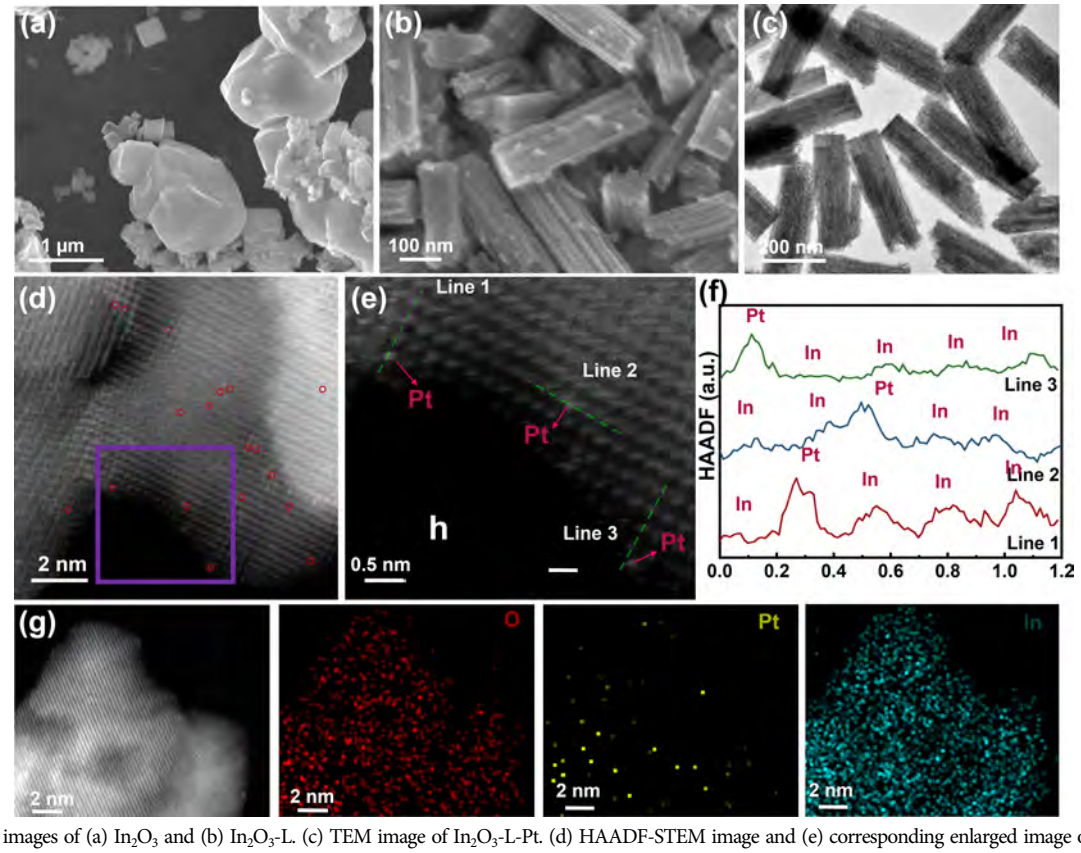


**Figure 2** SEM images of (a) $In_2O_3$ and (b) $In_2O_3$-L. (c) TEM image of $In_2O_3$-L-Pt. (d) HAADF-STEM image and (e) corresponding enlarged image of $In_2O_3$-L-Pt. (f) HAADF intensity line profiles taken along the appropriately numbered lines indicated. (g) HAADF-STEM micrograph of $In_2O_3$-L-Pt and corresponding elemental mappings.

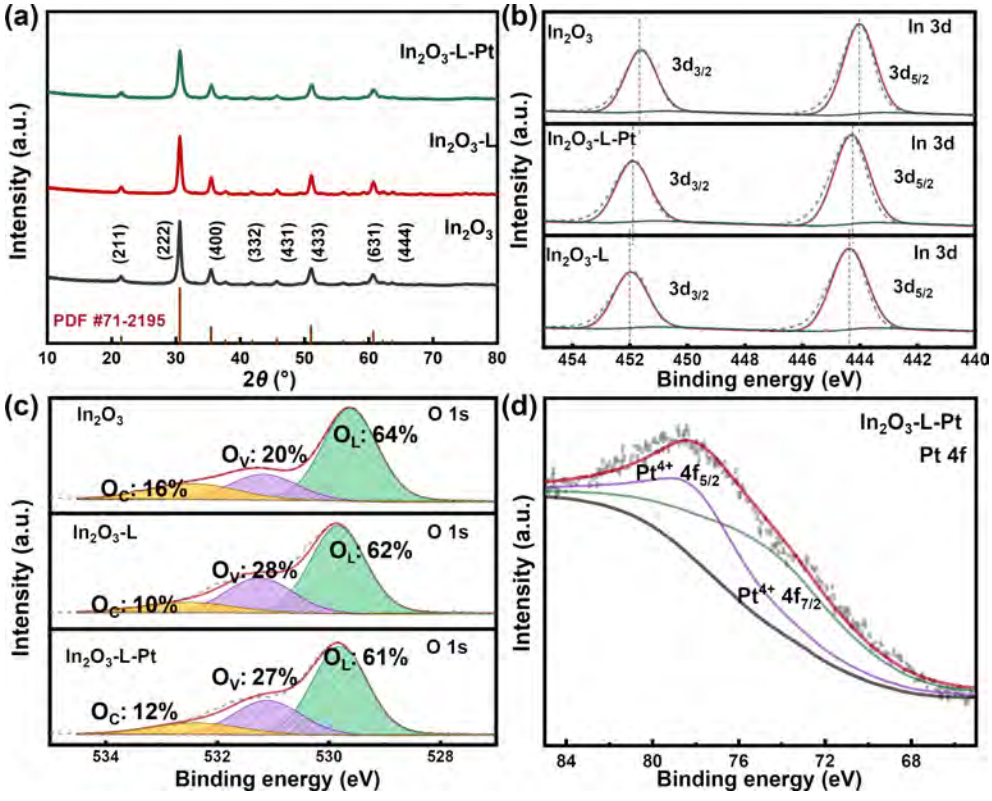


**Figure 3** (a) XRD spectra of $In_2O_3$, $In_2O_3$-L, and $In_2O_3$-L-Pt. XPS spectra of (b) In 3d, (c) O 1s and (d) Pt 4f of samples.

particles. Pt existed in a monatomic form, which was consistent with the previous TEM and HAADF-STEM results. The chemical composition and valence state of the samples were evaluated using XPS. The survey spectra showed that $In_2O_3$-L-Pt contained Pt, In, and O elements, but no Pt signal was detected in $In_2O_3$, indicating that the samples were successfully prepared (Fig. S4 in the ESM). In the XPS spectra of In 3d in $In_2O_3$-L, the two peaks were located at 444.4 ($3d_{5/2}$) and 451.9 eV ($3d_{3/2}$). However, the binding energy of In 3d in $In_2O_3$-L-Pt shifted negatively by 0.1 eV, indicating that electrons transferred from Pt to $In_2O_3$-L (Fig. 3(b)) [20, 21]. Compared with $In_2O_3$-L, the In 3d binding energy shifted to the right by 0.3 eV in $In_2O_3$, indicating that the preparation method affected the electronic structure. The spectra of O 1s showed that the peaks at 529.62, 531.16, and 523.43 eV belonged to lattice oxygen ($O_L$), vacancy oxygen ($O_V$), and adsorbed oxygen ($O_C$) respectively (Fig. 3(c)) [22]. Lattice oxygen in $In_2O_3$ accounted for 64% of the total oxygen signal, which was higher than that of oxygen vacancy (20%) and adsorbed oxygen species (16%). The vacancy concentrations of $In_2O_3$-L and $In_2O_3$-L-Pt ($O_V$ concentration: 28% and 27%, respectively) were higher than that of $In_2O_3$. The relative ratios of $O_V$ were $In_2O_3$-L-Pt:$In_2O_3$-L:$In_2O_3$ = 1.35:1.4:1. The construction of oxygen vacancies would increase the active sites on the material surface and improve the sensitivity performances. After loading Pt, the content of $O_V$ remained almost unchanged, indicating that the introduction of Pt into $In_2O_3$-L did not alter its morphological structure or the content of $O_V$. The Pt spectra showed that the diffraction peaks at 74.68 and 78.02 eV corresponded to Pt $4f_{7/2}$ and Pt $4f_{5/2}$, respectively, indicating that Pt existed in $In_2O_3$-L in the $Pt^{4+}$ oxidation state (Fig. 3(d)).

### 3.2 Investigation of gas-sensing performance

The gas sensitivity performance of the sample was tested through the gas sensitivity testing system. The performances of the fabricated sensors were assessed at different temperatures in 20 ppm acetone to study their optimal working temperature. The sensor sensitivities of samples exhibited a volcano-type relationship with the operating temperature. The response initially increased and then decreased with rising temperature, reaching a maximum at 220 °C (Fig. 4(a)). The initial increase in sensor sensitivity with operating temperature was attributed to the enhanced activity of $O_2$ and acetone molecules on the materials surface, which led to a greater change in charge carrier concentration, thereby increasing the sensor response. The initial increase of sensor response with temperature was attributed to the exponential acceleration of the reaction kinetics between acetone and surface oxygen species ($O^-$ and $O^{2-}$), which released more electrons into the $In_2O_3$-L-Pt conduction band and amplified the resistance change. Conversely, above the 220 °C, the response decreased because the thermodynamic equilibrium shifted towards desorption. The resulting decline in acetone surface coverage meant that fewer molecules were available for the reaction, making the rate-limiting step [23]. The resistance value of the samples decreased as the temperature rised, which was in line with the inherent characteristics of semiconductor materials (Fig. 4(c)). $In_2O_3$ and $In_2O_3$-L exhibited similar properties, while their optimal operating temperatures were 280 and 250 °C, respectively (Fig. S5 in the ESM). Comparative analysis of the sensing performances between the sensor fabricated in this work and other $In_2O_3$-based sensors is illustrated in Table S1 in the ESM.

The gas sensing properties of $In_2O_3$, $In_2O_3$-L, and $In_2O_3$-L-Pt with varying Pt contents were evaluated (Fig. S6 in the ESM). The results demonstrated that $In_2O_3$-L-Pt exhibited the highest response (Fig. 4(b)). It showed a response value of 16 at 220 °C, far surpassing that of $In_2O_3$ (response value: 3) and $In_2O_3$-L (response

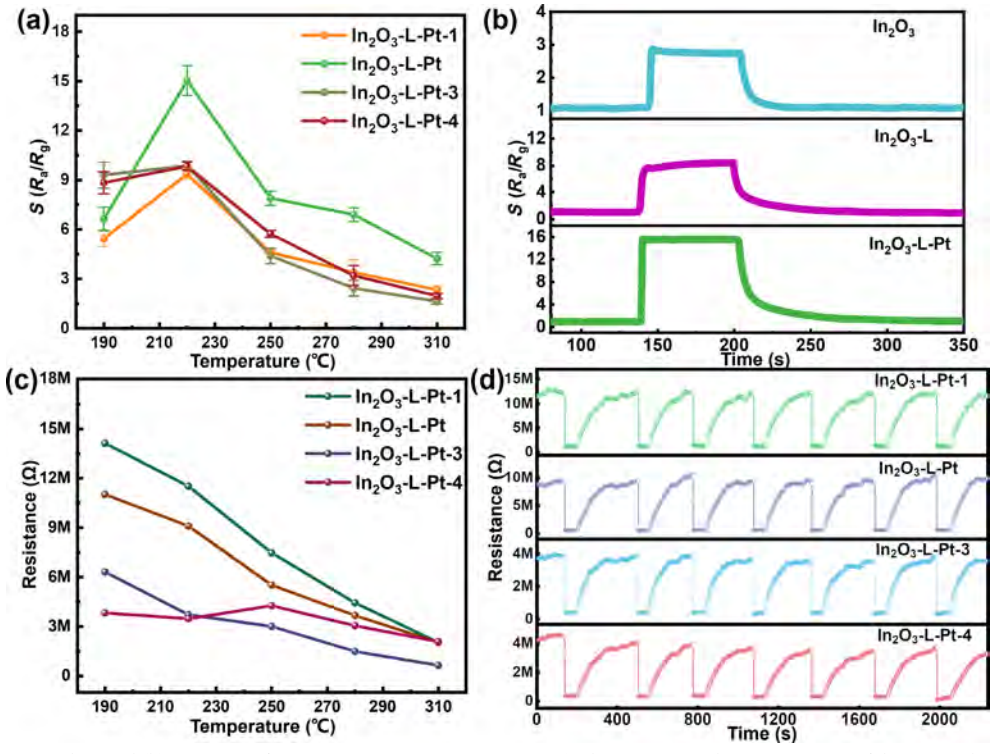


**Figure 4** (a) The response values and (b) resistance of sensors to 20 ppm at 190–310 ℃. (c) The response and recovery curves of the sensors based on $In_2O_3$, $In_2O_3$-L, and $In_2O_3$-L-Pt to 20 ppm acetone at 220 ℃. (d) The response and recovery curves of $In_2O_3$, $In_2O_3$-L, and $In_2O_3$-L-Pt sensors to 20 ppm acetone at 220 ℃.

value: 8). The improved response of the $In_2O_3$-L over $In_2O_3$ could be attributed to its larger surface area and abundant $O_V$, which provided more active sites for gas sensing [24, 25]. Furthermore, the incorporation of Pt into $In_2O_3$-L-Pt effectively promoted the adsorption and activation of oxygen molecules, and accelerated the redox reaction with acetone molecules. Pt acted as active sites lowered the energy barrier for acetone oxidation [26, 27], thereby significantly enhancing the sensing properties of the $In_2O_3$-L-Pt composite. The sensors also demonstrated excellent repeatability for 20 ppm acetone, as shown in Fig. 4(d). The response remained well-maintained with high reversibility and stability over multiple testing cycles. The dynamic resistance responses of the sensors to acetone concentrations ranging from 0.2 to 120 ppm were recorded to further investigate their sensing properties (Figs. 5(a)–5(d)). The sensing response of $In_2O_3$-L-Pt-1, $In_2O_3$-L-Pt, $In_2O_3$-L-Pt-3, and $In_2O_3$-L-Pt-4 increased significantly from 1.5/1.8/1.6/1.3 to 43.5/99.5/65.5/95.1 as the acetone concentration rose from 0.2 to 120 ppm. The sensitivities of the sensors escalated with increasing acetone concentration, demonstrating a pronounced response of approximately 1.8 even at a concentration as low as 200 ppb. As plotted in Fig. 5(e), the response values of $In_2O_3$-L-Pt exhibited an approximately linear relationship with the acetone concentration (Fig. S9 in the ESM). The sensing performances of $In_2O_3$-L-Pt-1, $In_2O_3$-L-Pt, $In_2O_3$-L-Pt-3, and $In_2O_3$-L-Pt-4 toward 20 ppm of various volatile organic compounds (VOCs) (including ammonia, aniline, ethylene glycol, trimethylamine, and triethylamine) were assessed at 220 ℃. As shown in Fig. 5(f), the $In_2O_3$-L-Pt sensor exhibited distinct selectivity and the highest sensitivity to acetone. Response and recovery time is critical performance metrics for gas sensors. As shown in Fig. 5(g), $In_2O_3$-L-Pt demonstrated superior performance to $In_2O_3$-L, with significantly shorter response and recovery time (about 2 vs. 30 s and 8 vs. 51 s) (Fig. S7 in the ESM). The incorporation of Pt into $In_2O_3$-L-Pt as a catalytic center facilitates the transport of charge carriers and accelerates the redox reaction with acetone. The $In_2O_3$-L sensor exhibited longer response and recovery time compared to $In_2O_3$ sensor. This phenomenon was attributed to the higher operating temperature of the $In_2O_3$ sensor, which promoted faster charge carrier migration. The long-term stability of the $In_2O_3$-L-Pt gas sensor was assessed over 30 days by repeatedly exposing it to 20 ppm acetone and air. As the relative humidity increases, the $In_2O_3$-L-Pt sensor exhibit a decline in response values (Fig. S8 in the ESM). The reason was that the increased concentration of water molecules consumed the surface actived oxygen species to form actived hydroxyl groups. Consequently, the sensitivity of the sensor decreased during the sensing process [28, 29]. As shown in Fig. 5(h), both the response value and the baseline resistance remained stable throughout this period, demonstrating excellent operational durability.

### 3.3 Early warning of acrylonitrile butadiene styrene (ABS) fires

ABS materials are widely used in cars [30–32]. Exposed to high temperatures, ABS materials would undergo thermal decomposition, releasing flammable gases such as ketones, which poses risks of fire and even explosion [33]. Based on the issue, we developed a highly sensitive acetone gas sensors ($In_2O_3$-L-Pt gas sensor), which could accurately detect the ketone gases produced during the thermal decomposition of ABS, enabling fire warning. The system integrated a wireless communication module, which transmitted data in real time to the cloud platform via the message queuing telemetry transport (MQTT) protocol, and simultaneously activated the sound and light alarm devices (Figs. 6(a) and 6(b)). The heating process was achieved by adjusting a variable potentiometer on the circuit board, which regulated the current

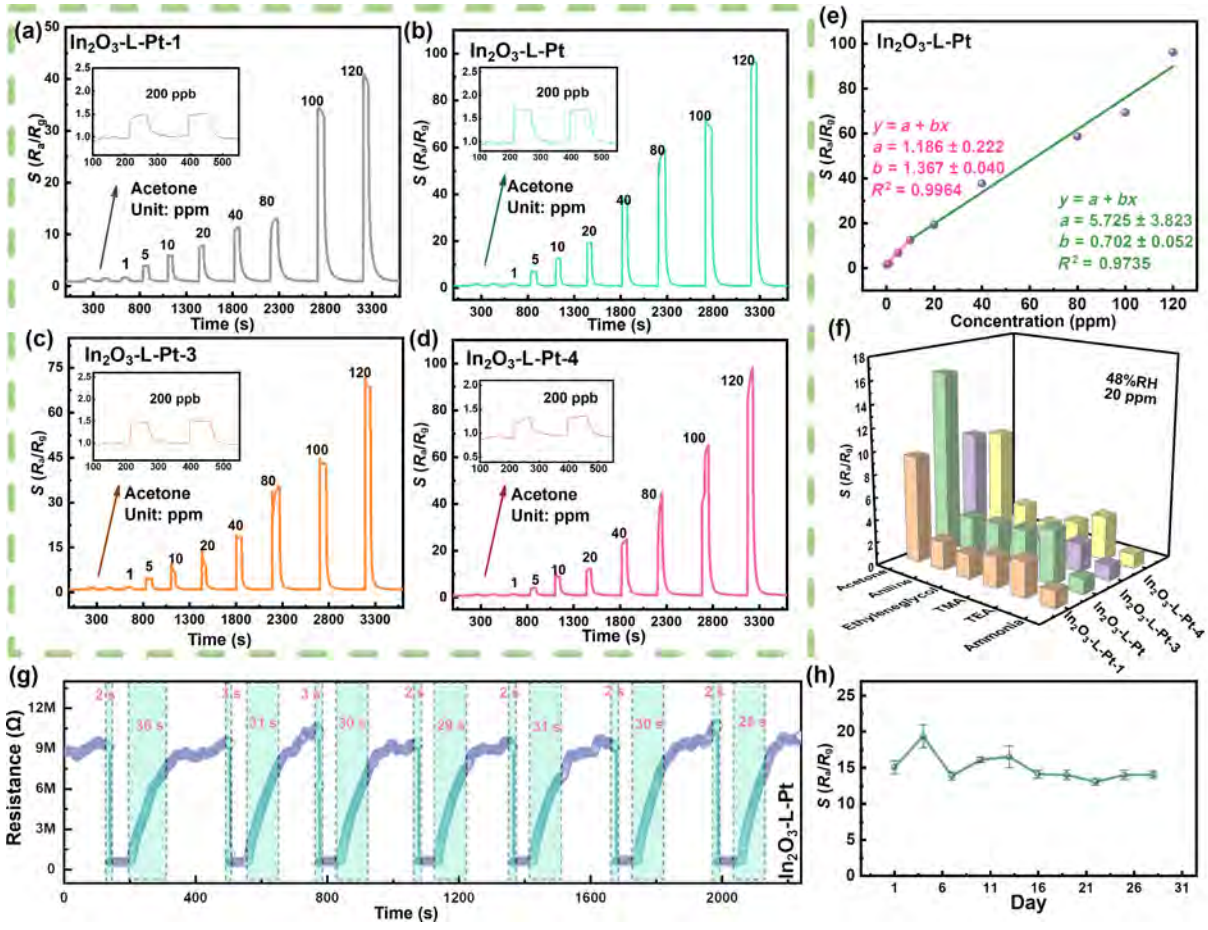


**Figure 5** The response and recovery curves of (a) $In_2O_3$-L-Pt-1, (b) $In_2O_3$-L-Pt, (c) $In_2O_3$-L-Pt-3, and (d) $In_2O_3$-L-Pt-4 sensor to various acetone concentrations at 220 °C. (e) The relationship between response values and acetone concentrations for $In_2O_3$-L-Pt sensor. (f) Sensing selectivity of $In_2O_3$-L-Pt-1, $In_2O_3$-L-Pt, $In_2O_3$-L-Pt-3, and $In_2O_3$-L-Pt-4 sensors to different target gases with concentration of 20 ppm. (g) The response and recovery curves of $In_2O_3$-L-Pt sensor to 20 ppm acetone at 220 °C. (h) The stability tests of $In_2O_3$-L-Pt to 20 ppm acetone.

through the sensor heating filament. The sensor reached its operating temperature, which was further confirmed using an infrared camera (Fig. S10 in the ESM). Exposing the $In_2O_3$-L-Pt gas sensor to an atmosphere generated by the thermal decomposition of ABS at different temperatures, the sensing performances of the sensor for early fire warning were evaluated (Fig. S11 in the ESM). The sensor was evaluated in a simulated automotive environment containing 30 g of ABS at 30–240 °C, as illustrated in Fig. 6(c). The sensor exhibited a rapid response, and the signal intensity showed a positive correlation with the temperature. This constructed a real-time remote fire monitoring and early warning system suitable for automotive environments, which is expected to provide security for drivers and passengers.

### 3.4 Sensing mechanism and discussion

The sensing performance of $In_2O_3$ gas sensor was determined by the processes of gas adsorption, dissociation, and conversion on its surface [34–36]. The sensing mechanism of metal oxide gas sensors primarily involved the redox reaction between target gas molecules and activated oxygen species. The oxygen species were activated into distinct states depending on the operating temperature of the sensor, such as $O_2^-$ (< 100 °C), $O^-$ (100–300 °C), and $O^{2-}$ (> 300 °C) [17, 37–39]. This initial step of the sensing process involved the electrons from the material conduction band to form species $O^-$, which established a electron depletion layer (EDL). The electrical resistance of the sensing materails underwent a change (Fig. 7(a)). Following contact with acetone molecules, the sensing process proceeded to the second stage, where a redox reaction occured between the $O^-$ species on the material surface and the target gas (Eq. (3)). Large number of electrons released from the reaction return to the band gap of the material, causing the EDL to rapidly narrow, which led to a decrease of the sensor resistance (Fig. 7(b)) [40–42]. When the sensor was removed from the acetone atmosphere, the sensing process entered the third stage. The reactive oxygen species recovered the surface of the material, captured electrons from the band gap, and further expanded the EDL, thereby restoring the sensing material to its initial state.

$$CH_3COCH_3 + 8O^- = 3CO_2 + 3H_2O + 8e^- \quad (3)$$

The $In_2O_3$-L possessed a larger specific surface area and a higher concentration of $O_V$ than that of $In_2O_3$, which enhanced the adsorption of activated oxygen species on the $In_2O_3$-L surface. The formation of oxygen vacancies will create a local electron-rich region. Many electrons were released back into the EDL of $In_2O_3$-L during an oxidation–reduction reaction with acetone, which led to a more significant changes in $In_2O_3$-L resistance and an improved the sensing sensitivity. Compared to $In_2O_3$-L, the Pt element has a higher work function, electron transferred from $In_2O_3$-L to the single-atom Pt sites [43]. To balance the Fermi levels of the $In_2O_3$-L

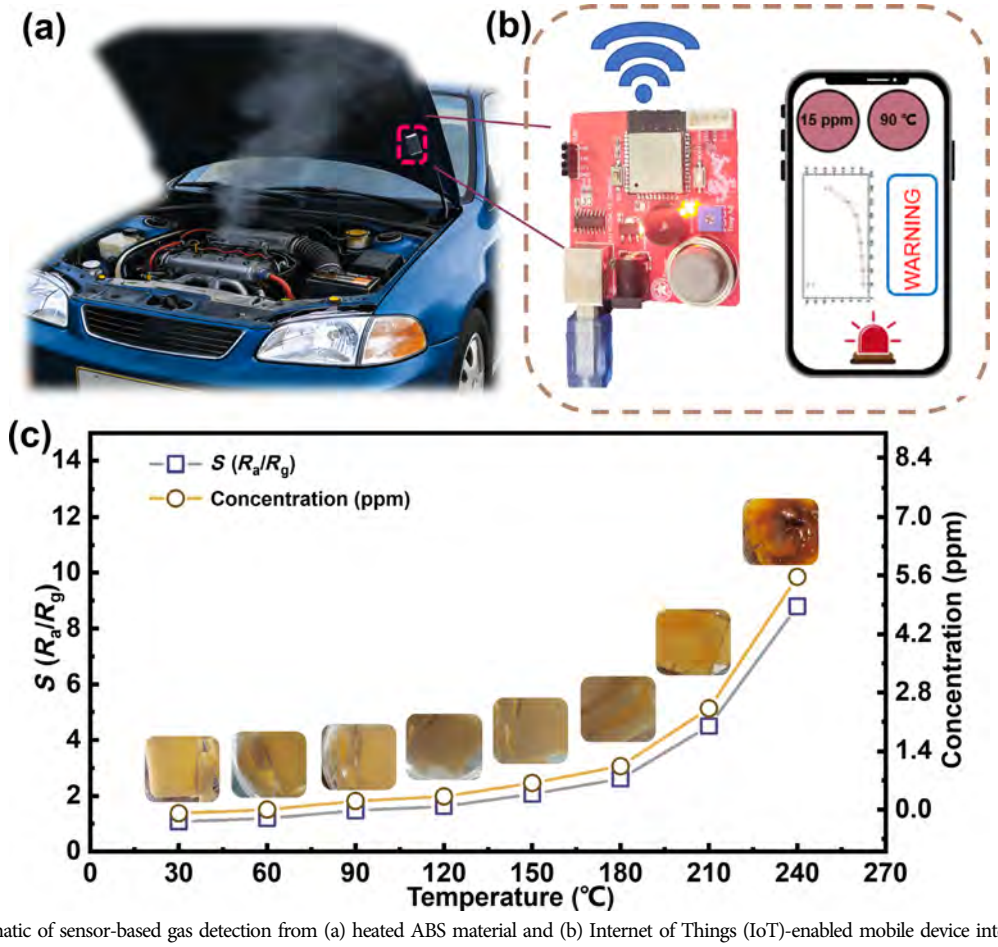


**Figure 6** The schematic of sensor-based gas detection from (a) heated ABS material and (b) Internet of Things (IoT)-enabled mobile device interconnection. (c) The dynamic response curve to gas release from heated material ABS.

and Pt, $In_2O_3$-L-Pt formed a thicker EDL, resulting in a significant increase in the initial resistance. The released electrons during the oxidation–reduction reaction with acetone could effectively reduce the EDL thickness. Meanwhile, the Pt could also serve as active sites for catalyzing the redox reactions on the material surface, resulting in a larger change in resistance than that of $In_2O_3$-L, thereby significantly enhancing the sensitivity of $In_2O_3$-L-Pt.

The sensing performance mechanism of the materials was further investigated by using DFT calculations. Figure 8(a) shows that $In_2O_3$-L-Pt had a lower adsorption energy (−0.89 eV) than that of $In_2O_3$ (0.30 eV) and $In_2O_3$-L (−0.11 eV), indicating that $In_2O_3$-L-Pt had a greater ability to adsorb acetone (Fig. 8(b)). The activation energy of $In_2O_3$-L-Pt (−0.69 eV) was much lower than that of $In_2O_3$ (0.30 eV) and $In_2O_3$-L (−0.41 eV), indicating that $In_2O_3$-L-Pt was more capable of activating acetone. The results demonstrated that $In_2O_3$-L-Pt had the best sensing performance, which was consistent with the results of the performance tests (Fig. 4(b)). Figure 8(c) reveals that the transferring 0.80 $e^-$ from the Pt atoms to $In_2O_3$-L induced a local concentration of electron density at the interfaces. The charge redistribution established a stronger internal electric field [22]. The enhancement of the electric field led to much free electrons of $In_2O_3$-L being unable to freely migrate, thereby significantly increasing the thickness of EDL and increasing the resistance of the sensing material. It was consistent with the test results (Fig. 4(c)). The acetone molecules transferred 0.10 $e^-$, 0.40 $e^-$, and 1.86 $e^-$ to $In_2O_3$, $In_2O_3$-L, and $In_2O_3$-L-Pt, respectively (Figs. 8(d)–8(f)). It was demonstrated that the introduction of single atoms Pt and oxygen vacancies could effectively increase the transfer of electrons from acetone to the sensing materials, thereby enhancing the sensitivity of the sensing material, which was consistent with the results of the tests.

## 4 Conclusions

In summary, we synthesized single-atoms Pt anchored on the nanorod-shaped $In_2O_3$ for realizing acetone gas detection. The $In_2O_3$-L-Pt sensor demonstrated an excellent response for 20 ppm acetone, which was 5 times higher than that of the $In_2O_3$ gas sensor. The $In_2O_3$-L-Pt sensor had a rapid response/recovery time of 2/30 s toward 20 ppm. Moreover, the sensor also showed a practical detection limit of 0.2 ppm with a response of 1.8, good repeatability, long-term operating stability, and good selectivity. The nanorod-shaped morphology increased the surface area of the sensing material, which was beneficial for the adsorption and activation of oxygen. The introduction of Pt atoms increased the adsorption and reduced the activation energy barrier of acetone. And the introduction of Pt single atoms created a built-in electric field at the interface of $In_2O_3$-L-Pt, which increased its EDL thickness, enhanced the resistance change of the sensor during the sensing process, and improved the sensitivity. The field increased the EDL thickness, thereby amplifying the resistance variation during gas sensing and gaining a superior sensitivity. The simulation of real-time monitoring of volatile ketone gases during car fires verified that the developed sensor had potential for application in fire warning.

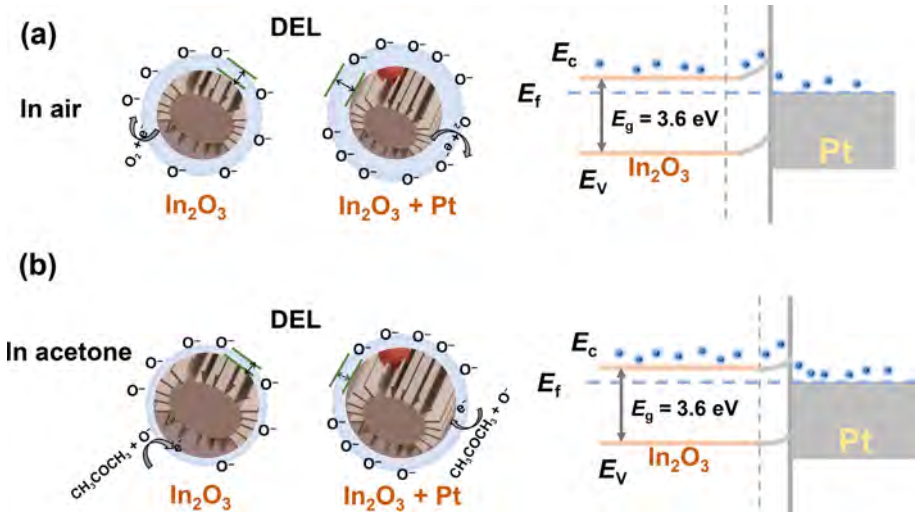


**Figure 7** Change of energy band and DEL of materials (in air and exposure to acetone).

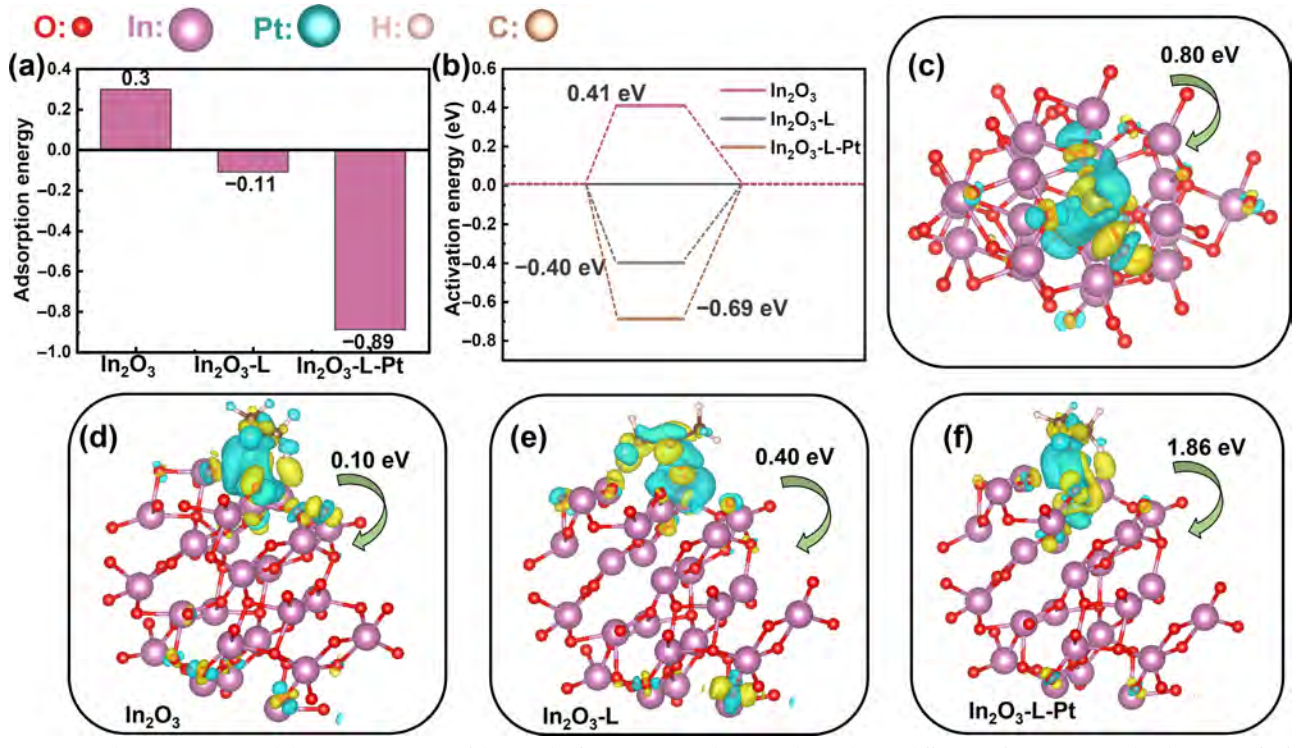


**Figure 8** (a) Adsorption energy and (b) activation energy of the samples for acetone. (c) Electronic charge density difference of $In_2O_3$-L-Pt. Bader charge transfer from acetone to (c) $In_2O_3$, (d) $In_2O_3$-L, and (f) $In_2O_3$-L-Pt (blue area: charge consumption, and yellow area: charge accumulation).

**Electronic Supplementary Material**: Supplementary material (sensor fabrication and testing details, SEM images, TEM images, XRD data, sensor performance tests at various temperatures, dynamic response of sensor resistance, recovery/response time measurement, humidity effect test, linear fitting of sensitivity vs. gas concentration, DFT calculation model, and comparison with the performances of previously reported materials) is available in the online version of this article at https://doi.org/10.26599/NR.2026.94908507.

## Data availability

All data needed to support the conclusions in the paper are presented in the manuscript and the Electronic Supplementary Material. Additional data related to this paper may be requested from the corresponding author upon request.

## Acknowledgements

This work was supported by the National Natural Science Foundation of China (Nos. 22508367 and 52171193), China Postdoctoral Science Foundation (No. 2024M762994), High-end Foreign Experts Recruitment Program of Henan Province (No. HNGD2023001), High-end Foreign Experts Recruitment Program of China (No. G2023026020L), Key Research and Development Program of Henan Province (No. 241111220400), the Plan for Zhongyuan Scientific Innovation Postdoctoral Talent of Henan Province (No.33220054), and the Key Laboratory of Automotive

Power Train and Electronics (Hubei University of Automotive Technology) (No. 2015XTZX0430).

## Declaration of competing interest

All the contributing authors report no conflict of interests in this work.

## Author contribution statement

J. M. G.: Writing – original draft, review & editing, data curation, and project administration Z. C. M.: Methodology, data curation, and investigation J. F. J.: Software. R. P. W. and H. G.: Investigation. K. H. S.: Resources. P. L., G. C. Q., and R. H. W.: Supervision. All the authors have approved the final manuscript.

## Use of AI statement

None.

## References

[1] González-Domínguez, R.; Sayago, A.; Akhatou, I.; Fernández-Recamales, Á. Volatile profiling of strawberry fruits cultivated in a soilless system to investigate cultivar-dependent chemical descriptors. *Foods* **2020**, *9*, 768.

[2] Majchrzak, T.; Wojnowski, W.; Wasik, A. Revealing dynamic changes of the volatile profile of food samples using PTR-MS. *Food Chem.* **2021**, *364*, 130404.

[3] Tan, J. Z.; Xu, J. Applications of electronic nose (e-nose) and electronic tongue (e-tongue) in food quality-related properties determination: A review. *Artif. Intell. Agric.* **2020**, *4*, 104–115.

[4] van den Broek, J.; Abegg, S.; Pratsinis, S. E.; Güntner, A. T. Highly selective detection of methanol over ethanol by a handheld gas sensor. *Nat. Commun.* **2019**, *10*, 4220.

[5] Gai, L. Y.; Lai, R. P.; Dong, X. H.; Wu, X.; Luan, Q. T.; Wang, J.; Lin, H. F.; Ding, W. H.; Wu, G. L.; Xie, W. F. Recent advances in ethanol gas sensors based on metal oxide semiconductor heterojunctions. *Rare Met.* **2022**, *41*, 1818–1842.

[6] Jiang, B.; Lu, J. Y.; Han, W. J.; Sun, Y. F.; Wang, Y. L.; Cheng, P. F.; Zhang, H.; Wang, C.; Lu, G. Y. Hierarchical mesoporous zinc oxide microspheres for ethanol gas sensor. *Sens. Actuators B: Chem.* **2022**, *357*, 131333.

[7] Umar, A.; Hussain, S.; Ansari, S. A.; Ibrahim, A. A.; Alhamami, M. A. M.; Almas, T.; Akbar, S. Indium oxide nanocubes for enhanced ethanol gas sensing and photocatalytic applications. *Ceram. Int.* **2025**, *51*, 16037–16045.

[8] Zhang, K.; Qin, S. W.; Tang, P. G.; Feng, Y. J.; Li, D. Q. Ultra-sensitive ethanol gas sensors based on nanosheet-assembled hierarchical ZnO–$In_2O_3$ heterostructures. *J. Hazard. Mater.* **2020**, *391*, 122191.

[9] Deng, Y.; Liu, Y.; Deng, Y. H.; Cheng, J. S.; Zou, Y. D.; Luo, W. *In situ* sulfur-doped mesoporous tungsten oxides for gas sensing toward benzene series. *Chin. Chem. Lett.* **2024**, *35*, 108898.

[10] Shuvo, S. N.; Ulloa Gomez, A. M.; Mishra, A.; Chen, W. Y.; Dongare, A. M.; Stanciu, L. A. Sulfur-doped titanium carbide MXenes for room-temperature gas sensing. *ACS Sens.* **2020**, *5*, 2915–2924.

[11] Li, Z. K.; Wu, X.; Wang, W.; Wen, X. M.; Niu, F.; Han, D. D.; Zhong, W.; Ordomsky, V. V.; Wang, Q. Y.; Wei, R. et al. Monolayer amphiphiles hydrophobicize $MoS_2$-mediated real-time water removal for efficient waterproof hydrogen detection. *ACS Sens.* **2024**, *9*, 6430–6440.

[12] Hou, X. Y.; Liu, H. H.; Zhang, Y. M.; Jiang, M. P.; Yuan, L.; Shi, J. Y.; Hou, C. M. Oxygen vacancies enhancing acetone-sensing performance. *Mater. Today Chem.* **2020**, *18*, 100372.

[13] Hussain, M. B.; Kang, B. K.; Cheng, X. X.; Ma, C. Y.; Wang, X. T.; Mehmood, R.; Iqbal, S. Oxygen vacancy induced Pt-decorated MOF photocatalyst for hydrogen production. *Int. J. Hydrogen Energy* **2023**, *48*, 13780–13790.

[14] Zhang, Y.; Hang, C.; Jiang, H. C.; Zhao, X. H.; Deng, X. W.; Wang, L. F.; Ma, F. X.; Xu, Z. J. Introducing oxygen vacancies into $WO_3$ thin film for improving hydrogen sensing performance of Pd/$WO_{3-x}$/AAO sensors. *Sens. Actuators B: Chem.* **2025**, *423*, 136843.

[15] Yang, Y.; Xie, Y. Y.; Liu, J. C.; Wang, H.; Li, X. W.; Zhou, T.; Sun, F. Z.; Feng, Z. Y.; Wang, X. M.; Jia, F. C. Transition metals (Fe/Mn)-doped g-$C_3N_4$ and ZnO nanosheet composite sensors for efficient detection of BTEX. *Sens. Actuators B Chem.* **2025**, *428*, 137251.

[16] Tagliaferro, J. C.; Komorizono, A. A.; Pessoa, N. C. S.; Correia, R. S.; Bernardi, M. I. B.; Mastelaro, V. R. Influence of morphology and heterostructure formation on the $NO_2$ gas sensing properties of the ZnO-NiO system. *Talanta Open* **2024**, *10*, 100388.

[17] Shin, H.; Jung, W. G.; Kim, D. H.; Jang, J. S.; Kim, Y. H.; Koo, W. T.; Bae, J.; Park, C.; Cho, S. H.; Kim, B. J. et al. Single-atom Pt stabilized on one-dimensional nanostructure support via carbon nitride/$SnO_2$ heterojunction trapping. *ACS Nano* **2020**, *14*, 11394–11405.

[18] Talib, S. H.; Jiang, X. L.; Feng, S. X.; Zhao, M. D.; Yu, Q. Theoretical catalytic performance of single-atom catalysts $M_1/PW_{12}O_{40}$ for alkyne hydrogenation materials. *Nano Res. Energy* **2024**, *3*, e9120128.

[19] Talib, S. H.; Ali, B.; Dar, A. H.; Qurashi, A.; Li, J.; Mohamed, S. Catalytic reduction of $N_2O$ by CO molecules using transition metal-phosphomolybdic acid ($TM_1$/PMA) single-atom catalysts: A theoretical perspective. *Nano Res. Energy* **2025**, *4*, e9120158.

[20] Xi, Z.; Erdosy, D. P.; Mendoza-Garcia, A.; Duchesne, P. N.; Li, J. R.; Muzzio, M.; Li, Q.; Zhang, P.; Sun, S. H. Pd nanoparticles coupled to $WO_{2.72}$ nanorods for enhanced electrochemical oxidation of formic acid. *Nano Lett.* **2017**, *17*, 2727–2731.

[21] Peng, L. X.; Tian, H.; Cui, X. Z.; Su, L.; Meng, G.; Ma, Z. H.; Cao, S. W.; Shi, J. L. Dual synergetic catalytic effects boost hydrogen electric oxidation performance of Pd/$W_{18}O_{49}$. *Nano Res.* **2021**, *14*, 2441–2450.

[22] Zhang, S. C.; Chang, X.; Zhou, L. H.; Liu, X. H.; Zhang, J. Stabilizing single-atom Pt on $Fe_2O_3$ nanosheets by constructing oxygen vacancies for ultrafast $H_2$ sensing. *ACS Sens.* **2024**, *9*, 2101–2109.

[23] Wang, H. C.; Zhang, H.; Zhang, J. J.; Han, J. P.; Fang, H.; Yu, M. H.; Chang, Z.; Bu, X. H. Innovative microstructure and morphology engineering of MOF-derived single-Atom Sn-doped ZnO nanosheet showing highly sensitive acetone sensing. *Adv. Funct. Mater.* **2025**, *35*, 2422378.

[24] Jiang, B.; Zhou, T. T.; Zhang, L.; Han, W. J.; Yang, J. Q.; Wang, C.; Sun, Y. F.; Liu, F. M.; Sun, P.; Lu, G. Y. Construction of mesoporous $In_2O_3$-ZnO hierarchical structure gas sensor for ethanol detection. *Sens. Actuators B: Chem.* **2023**, *393*, 134203.

[25] Wang, J.; Ni, Y. J.; Li, X. B.; Jiang, X. Q.; Jin, Q. H.; Zhang, X.; Wei, S. H.; Jin, H.; Yuan, T.; Zou, J. et al. Enhancement of nitric oxide sensing performance via oxygen vacancy promotion on strontium-doped $LaFeO_3$ perovskites. *Sens. Actuators B: Chem.* **2024**, *417*, 136157.

[26] Natkaeo, A.; Phokharatkul, D.; Hodak, J. H.; Wisitsoraat, A.; Hodak, S. K. Highly selective sub-10 ppm $H_2S$ gas sensors based on Ag-doped $CaCu_3Ti_4O_{12}$ films. *Sens. Actuators B: Chem.* **2018**, *260*, 571–580.

[27] Wang, Y.; Wang, Y. M.; Cao, J. L.; Kong, F. H.; Xia, H. J.; Zhang, J.; Zhu, B. L.; Wang, S. R.; Wu, S. H. Low-temperature $H_2S$ sensors based on Ag-doped α-$Fe_2O_3$ nanoparticles. *Sens. Actuators B: Chem.* **2008**, *131*, 183–189.

[28] Mu, Y.; Yue, Q.; Chen, X. T.; Chen, Q. Y.; Qu, J. Y.; Guo, Y. J.;

Dastan, D.; Yin, X. T.; Ma, X. G. Construction of heterojunction based on $Nd_2S_3$ and tin dioxide for rapid detection of ethanol. *Sens. Actuators B: Chem.* **2025**, *423*, 136829.

[29] Wang, Z. Z.; Li, P.; Feng, B. X.; Feng, Y. Y.; Cheng, D.; Wei, J. Wireless gas sensor based on the mesoporous ZnO–$SnO_2$ heterostructure enables ultrasensitive and rapid detection of 3-methylbutyraldehyde. *ACS Sens.* **2024**, *9*, 2585–2595.

[30] Alonso, A.; Lázaro, M.; Lázaro, D.; Alvear, D. Thermal characterization of acrylonitrile butadiene styrene-ABS obtained with different manufacturing processes. *J. Therm. Anal. Calorim.* **2023**, *148*, 10557–10572.

[31] Li, M. Z.; Wang, W.; Yu, J. Comparison of the pyrolysis behavior of PC, ABS and PC/ABS. *J. Anal. Appl. Pyrolysis* **2024**, *183*, 106774.

[32] Ramirez, N. V.; Sanchez-Soto, M. Effects of poss nanoparticles on ABS–g–Ma thermo oxidation resistance. *Polym. Compos.* **2012**, *33*, 1707–1718.

[33] Xu, L.; Li, S. C.; Zhang, Y. C.; Sun, W. H.; Pan, L. W.; Wang, L. Non-isothermal thermal decomposition behavior and reaction kinetics of acrylonitrile butadiene styrene (ABS). *J. Environ. Manage.* **2023**, *348*, 119080.

[34] Li, L.; Hong, D. C.; Liu, B. H.; Su, T. C.; Yang, X. L.; Yue, L.; Zhang, W. H. Porous Zn-doped $In_2O_3$ nanobelts for ppb level acetone sensing at low operating temperature. *Sens. Actuators B: Chem.* **2025**, *433*, 137451.

[35] Lin, X. R.; Chen, R. J.; Zhong, Q. H.; Yang, X. Y.; Sun, B. T.; Hu, R. M.; Song, P. Synthesis of Ni-doped perovskite $LaFeO_3$ nanofibers and their gas-sensing performance for ethanolamine. *J. Environ. Chem. Eng.* **2025**, *13*, 120425.

[36] Zhao, F.; Yu, L. M.; Wang, J. F.; Cao, W.; Zhang, H.; Wang, H. R.; Wang, P. H.; Qiao, Z. H. Metal-organic framework-derived Au-doped $In_2O_3$ nanotubes for monitoring CO at the ppb level. *ACS Sens.* **2024**, *9*, 4007–4016.

[37] Xu, J. H.; Zhao, H. Y.; Guo, Y. J.; Qu, J. Y.; Chen, X. T.; Wang, X. N.; Dastan, D.; Tan, X. M.; Yin, X. T.; Ma, X. G. Exceptional enhancement of response and stability in ethanol sensors based on Pr-doped $In_2O_3$. *Sens. Actuators B: Chem.* **2026**, *449*, 139147.

[38] Gao, Y. F.; Wang, X. H.; Zhang, Q. B.; Wang, H. Y.; Xu, G. G.; Wang, X. Z. Influence of La doping on the ethanol gas sensing properties of $CdSnO_3$ micro-cubes. *Sens. Actuators B: Chem.* **2023**, *394*, 134447.

[39] Fan, G. J.; Guan, J.; Yu, H.; Zhu, Q. Y.; Han, N.; Mo, J. H.; Chen, Y. F. Highly sensitive formaldehyde gas sensor based on $SnO_2$/$Zn_2SnO_4$ hybrid structures. *Build. Environ.* **2024**, *262*, 111781.

[40] Li, C. Y.; Choi, P. G.; Kim, K.; Masuda, Y. High performance acetone gas sensor based on ultrathin porous NiO nanosheet. *Sens. Actuators B: Chem.* **2022**, *367*, 132143.

[41] Bulemo, P. M.; Cheong, J. Y. MOF-derived $SnO_2$ hollow spheres for acetone gas sensing. *J. Mater. Sci.: Mater. Electron.* **2023**, *34*, 1060.

[42] Zhang, C. M.; Wu, X. Y.; Zha, C.; Li, L.; Lu, H.; Chen, T.; Zhang, S.; Xing, H. H.; Zhao, M. D.; Sun, W. et al. MXene/$Co_3O_4$ layered composites for acetone gas sensing. *ACS Appl. Nano Mater.* **2024**, *7*, 20690–20699.

[43] Liu, H.; Liu, Q.; Feng, Y. J.; Xu, D. M.; Tang, P. G.; Li, D. Q. Facile assembly of Au nanoparticles modified hierarchical mesoporous $In_2O_3$ for highly sensitive ethanol gas detection. *Sens. Actuators B: Chem.* **2024**, *402*, 135103.